Design, Fabrication, and Characterization of a Rotary Micromotor Supported on Microball Bearings

Nima Ghalichechian, *Student Member, IEEE*, Alireza Modafe, *Student Member, IEEE*, Mustafa Ilker Beyaz, *Student Member, IEEE*, and Reza Ghodssi, *Member, IEEE*

***Abstract*—We report the design, fabrication, and characterization of a rotary micromotor supported on microball bearings. This is the first demonstration of a rotary micromachine with a robust mechanical support provided by microball-bearing technology. A six-phase bottom-drive variable-capacitance micromotor ($\phi = 14$ mm) is designed and simulated using the finite-element (FE) method. The stator and the rotor are fabricated separately on silicon substrates and assembled with the microballs. Three layers of low-k benzocyclobutene polymer, two layers of gold, and a silicon microball housing are fabricated on the stator. Microball housing and salient structures (poles) are etched in the rotor and are coated with a silicon carbide film that reduces the friction without which the operation was not possible. A top angular velocity of 517 r/min, corresponding to the linear tip velocity of 324 mm/s, is measured at $\pm$150-V and 800-Hz excitation. This is 44 times higher than the velocity previously demonstrated for linear micromotors supported on the microball bearings. A noncontact method is developed to extract the torque and the bearing coefficient of friction through dynamic response measurements. The torque is indirectly measured to be -5.62 ± 0.5 μN $\cdot$ m at $\pm$150-V excitation which is comparable with the FE simulation results predicting -6.75 μN $\cdot$ m. The maximum output mechanical power at $\pm$150 V and 517 r/min was calculated to be 307 μW. The bearing coefficient of friction is measured to be 0.02 ± 0.002 which is in good agreement with the previously reported values. The rotary micromotor developed in this paper is a platform technology for centrifugal micropumps used for fuel-delivery and cooling applications. [2007-0216]**

***Index Terms*—Microball bearings, micromotor, variable capacitance.**

I. Introduction

MICROMOTORS and microgenerators are power microelectromechanical systems (MEMS) for energy conversion between mechanical and electrical domains. A robust rotary micromotor can be used as a platform for developing micropumps which are highly demanded microsystems for fuel-delivery, drug-delivery, cooling, and vacuum applications [1]–[4]. Micromotors can also be employed in microscale surgery [5], [6], assembly [7], propulsion, and actuation [8], [9].

Various types of micromachines have been successfully fabricated and tested in the past. A variable-capacitance micromotor (VCM) supported on center-pin (bushing) bearings with 12 pN $\cdot$ m of torque [10], an electric induction micromotor supported on gas-lubricated bearings with 3.5 μN $\cdot$ m of torque [11], [12], and a magnetic induction micromotor with a tethered rotor and 2.5 μN $\cdot$ m of torque [13] are a few examples. Furthermore, an electric induction microgenerator supported on gas-lubricated bearings was reported to generate 108 μW of electric power [14]; a permanent magnet microgenerator with an external support (spindle shaft) was reported to generate 8 W [15], [16].

One key challenge in the realization of reliable micromotors and microgenerators is the development of a support mechanism for the rotor that would result in high stability, low friction, and high resistance to wear. The center-pin design, which is used in conventional micromotors, results in friction, wear, fracture, stiction, and contamination-based failure modes [17]. The gas-lubricated bearings [18], [19], which are utilized in high-speed applications, suffer from stability limits and require complex control schemes and fabrication processes using a stack of bonded wafers. Conversely, microball-bearing technology in silicon [20], [21] provides a reliable support mechanism for the rotor with high stability. This approach results in less friction and wear compared with the center-pin or flange designs used in conventional side-drive VCMs [10], [22]. Furthermore, the fabrication process of a microball-bearing-supported machine is less complicated than that of the gas-lubricated machines, and the rotor is more stable. Another advantage of this technology is the ability to define and sustain a uniform gap across the active area of the device. This requirement is significant for electrostatic micromachines for two reasons, i.e., the air gap needs to be small, and the active area must be large to maximize the torque.

Being composed of conductors and dielectrics, the VCMs, unlike magnetic machines, are fabricated using conventional micromachining techniques. The energy density of these voltage-driven machines is limited by the breakdown electric field at the gap, whereas the magnetic machines are limited by the saturation current. The device reported here, unlike the conventional VCMs, has a bottom-drive design to increase the active area. Therefore, compared with the conventional

Manuscript received September 4, 2007; revised November 6, 2007. This work was supported in part by the Army Research Laboratory under Grant CAW911NF-05-2-0026, by the Army Research Office under Grant ARMY-W911NF0410176, and by the National Science Foundation under Grant ECS-0224361. Subject Editor R. Howe.

N. Ghalichechian was with the MEMS Sensors and Actuators Laboratory, Department of Electrical and Computer Engineering, Institute of Systems Research, University of Maryland, College Park, MD 20742 USA. He is now with Formfactor Inc., Livermore, CA 94551 USA.

A. Modafe was with the MEMS Sensors and Actuators Laboratory, Department of Electrical and Computer Engineering, Institute for Systems Research, University of Maryland, College Park, MD 20742 USA. He is now with the Micron Technology Inc., Manassas, VA 20110 USA.

M. I. Beyaz and R. Ghodssi are with the MEMS Sensors and Actuators Laboratory, Department of Electrical and Computer Engineering, Institute for Systems Research, University of Maryland, College Park, MD 20742 USA.

Color versions of one or more of the figures in this paper are available online at http://ieeexplore.ieee.org.

Digital Object Identifier 10.1109/JMEMS.2008.916346

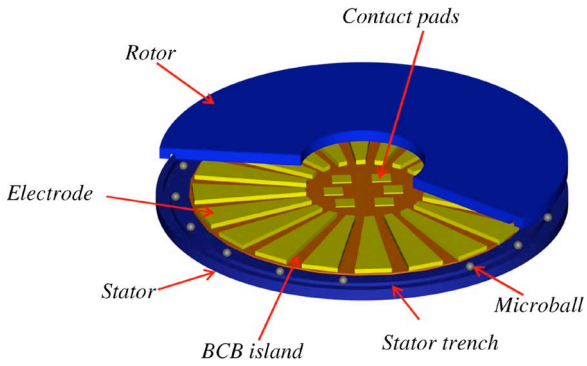

Fig. 1. Simplified 3-D schematic of the rotary micromotor. Dimensions are not to scale.

VCMs, the torque is increased by approximately three orders of magnitude; this has become possible by using microball bearings to maintain a small uniform gap between the rotor and the stator. The small gap size, however, imposes fabrication challenges that need to be addressed.

Previously, an *in situ* noncontact experimental setup was used in our group to study the frictional behavior of the microballs in the microscale regime. The static and dynamic coefficients of friction between stainless-steel microballs and silicon grooves were measured to be 0.01 and 0.007, respectively [20], [23], compared with 0.01–0.08 reported for silicon–silicon structures.

Realization of the rotary micromotor reported in this paper is based on our previous work on linear micromotors. The design, fabrication, and testing of the first [24] and the second [25] generations of bottom-drive linear VCMs supported on the stainless-steel microballs were previously reported by our group. In the second generation, slider displacement, instantaneous and average velocities, acceleration, and net force were obtained using a high-speed camera data-acquisition system. An average linear velocity of 7.2 mm/s was achieved at 120-V and 60-Hz excitation and was in agreement with the predicted value. A modeling scheme based on a mass–dashpot–spring system was also reported. The results obtained from the development of the linear device, together with the electrical characterization of the low-k dielectric used in the structure of the motor [26], process developments [26], [27], and interface studies [27], were implemented in the development of the rotary machine.

The rotary micromotors, compared with their linear counterparts, have a wider range of applications. In this paper, we first report the design and simulation of the rotary device followed by the fabrication, testing, and discussion. The device is the first demonstration of a rotary micromotor using the microball-bearing technology.

II. Design and Simulation

The micromotor reported in this paper is a six-phase bottom-drive rotary variable-capacitance machine with a robust mechanical support provided by the microball bearings. Fig. 1 shows the simplified 3-D schematic of the device composed of three components: rotor ($\phi = 14$ mm), stator, and stainless-steel microballs ($\phi = 284.5 \pm 0.25$ μm) [28]. The rotor is a silicon disc ($\rho = 1 - 10$ $\Omega \cdot$ cm) with microball housing and salient structures etched in silicon. The conductivity of silicon was chosen such that the substrate maintains a uniform ground potential during the operation of the device. The stator is a silicon disc (with identical properties as rotor) that includes microball housing and active parts, i.e., conductors and dielectrics. Electrodes/poles on the stator/rotor have the same width; however, they have a different spacing which results into 6 : 4 pole-to-electrode ratio. When a potential is applied to an electrode, image charges are induced on an adjacent pole, resulting in tangential and normal forces. The tangential force is the propelling force of the rotor which aligns a rotor pole to an adjacent active electrode. The normal force assists to hold the rotor on the stator. Continuous motion of the rotor is possible by sequential excitation of the electrodes with positive square pulses in a three-phase configuration (e.g., A, B, and C); each is 120° apart. To prevent charge buildup on the rotor, the second group of phases (D, E, and F) is excited with negative amplitude and identical phase to the first three.

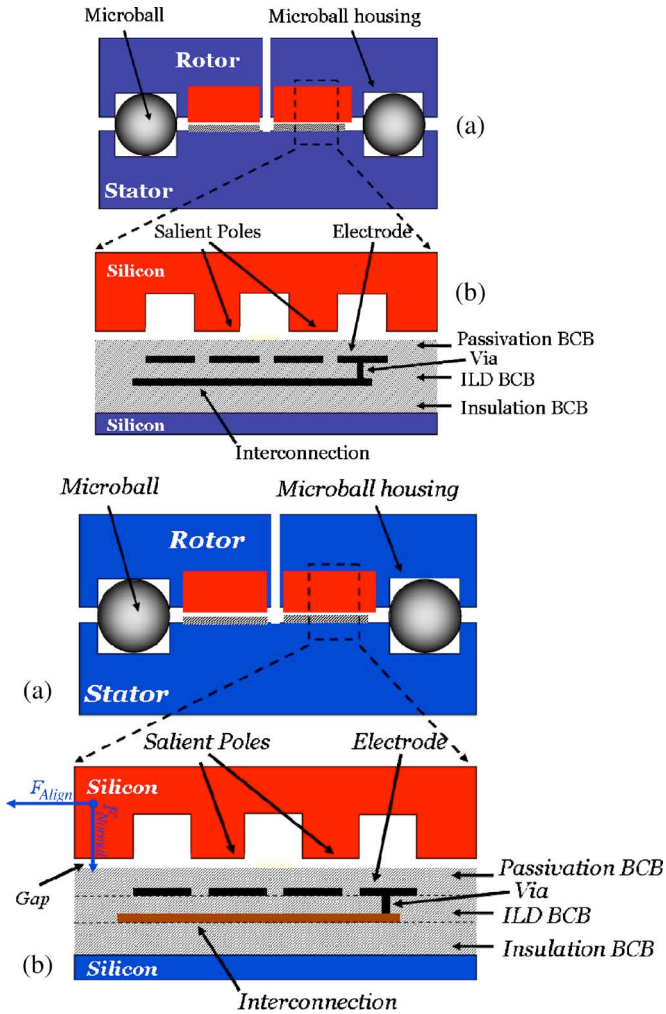

Fig. 2. Schematic (a) radial cross section of the mechanical (bearing) and electrical (active) components of the micromachine and (b) azimuthal cross section of the stator and rotor active pars.

Fig. 2 shows the schematic cross section of the motor. Various layers on the stator are shown in this figure. A layer

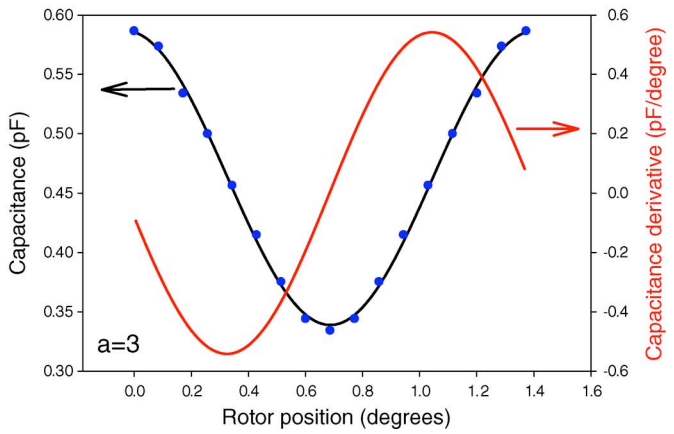

Fig. 3. (Left axis) Capacitance and (right axis) derivative of the capacitance as a function of rotor angular position when the distance between two electrodes is 1/3 of the electrode width ($a = 3$ and $G = 10$ μm).

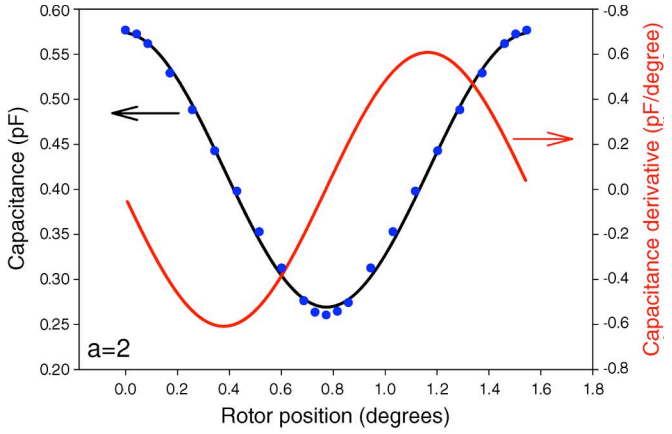

Fig. 4. (Left axis) Capacitance and (right axis) derivative of the capacitance as a function of rotor angular position when the distance between two electrodes is 1/2 of the electrode width ($a = 2$ and $G = 10$ μm).

of low-dielectric-constant benzocyclobutene (BCB) polymer film $(k = 2.65)$ is used for electrical isolation of the first metal layer (interconnection) from the silicon substrate. The interconnection layer connects every other six electrodes of the six-phase machine. The BCB film is used as an interlayer dielectric (ILD) between the two metal layers with vias providing electrical connection path between the two. The trapezoid-shaped electrodes are designed radially on top of the ILD with inner and outer radii of 1 and 5 mm, respectively. The final BCB layer is used for passivation. The BCB dielectric film, compared with the conventional silicon-dioxide-insulating films, reduces the parasitic capacitance between the electrodes and the stator substrate; therefore, the electrical efficiency of this micromotor is higher than that of the silicon-dioxide-based machines. In addition, the residual stress of the BCB film is lower than that of the silicon-dioxide film, resulting in less wafer curvature and better gap uniformity.

Six contact pads $(180 \times 180\ \mu\text{m}^2)$ are designed at the center of the stator such that they are easily accessible for probing through a 1-mm-radius rotor opening. The rotor is composed of etched silicon structures with a thin film of silicon carbide (SiC) for friction reduction. The fabrication processes for both the stator and the rotor are explained in the next section.

The torque (T) of the micromotor as a function of applied voltage (ν) and angular position of the rotor (θ) is derived to be

$$T(\nu,\theta) = \frac{-1}{12} N_e \nu^2 \left(\frac{\partial C_1(\theta)}{\partial \theta} + \frac{\partial C_2(\theta)}{\partial \theta} + \frac{\partial C_3(\theta)}{\partial \theta} \right) \quad (1)$$

where N_e is the number of electrodes on the stator, and $C(\theta)$ is the capacitance of a single electrode–pole pair. In (1), ν is given in volts, $\partial C(\theta)/\partial(\theta)$ is in farads over radian, and torque is in newton meter [29]. For a given geometry, torque can be analytically evaluated if $\partial C_n(\theta)/\partial\theta$ values are known. Finite-element (FE) method is used to simulate $C(\theta)$ and derive $\partial C_n(\theta)/\partial\theta$.

Fig. 3 shows the FE simulation results for the capacitance versus the angular position for a segment of the machine composed of six electrodes and four poles. The trapezoid-shaped electrodes and poles have the width (W) of 90 μm at the midpoint. The spacing between each electrode is determined by W/a, where "a" is an integer called the packing factor. The simulation results are shown for $a = 3$ which corresponds to the spacing of 30 μm at the midpoint between electrodes. The capacitance values are then fitted to the sine-squared function in the form of

$$C(\theta) = C_0 + a_1 \left[\sin\left(\frac{2\pi\theta}{a_2} + a_3 \right) \right]^2. \quad (2)$$

Fig. 3 also shows the fitted curve with the following constants: $C_0 = 0.33$ pF, $a_1 = 0.24$, $a_2 = 2.87$, and $a_3 = 1.63$. The standard coefficient of determination (R^2), describing how well a set of data points is fitted to a curve, is calculated to be 0.9999 which shows a good agreement between the fitted curve and the simulated data. By using the sine-squared curve fit, the first derivative is numerically calculated and shown on the right axis. Simulations were performed for a machine with the same geometry but with a packing factor of $a = 2$. The values of $C_0 = 0.26$ pF, $a_1 = 0.30$, $a_2 = 3.14$, and $a_3 = 1.59$ are obtained. Fig. 4 shows the capacitance variation results as well as the calculated derivative. Compared with the previous case, the derivative of capacitance for each segment of the machine with $a = 2$ is 25% higher than before. However, since the electrodes are loosely packed, the total number of electrodes is less.

To further analyze the effect of the packing factor and the gap size on the torque of the machine, a total of 24 simulations were performed at three different gap sizes (5, 10, and 15 μm) and four different packing factors (one, two, three, and four). For simplicity, only C_{Max} and C_{Min} are calculated. The derivative of capacitance is estimated using the linear approximation of $(C_{\text{Max}} - C_{\text{Min}})/(\theta_{\text{Max}} - \theta_{\text{Min}})$, where θ_{Max} and θ_{Min} are the rotor positions at full alignment and misalignment, respectively. Fig. 5 shows the summary of these simulations. The results for $a = 3$ and $a = 2$ (10-μm gap size) are in agreement with the previous method (less than 5% error). As expected, the torque of the machine increases by more than a factor of two when the gap is decreased from 10 to 5 μm. Fabrication imperfections will limit the implementation of such a small gap. In contrast, the torque is reduced when the gap is increased from 10 to 15 μm; however, fabrication of a machine with a gap of

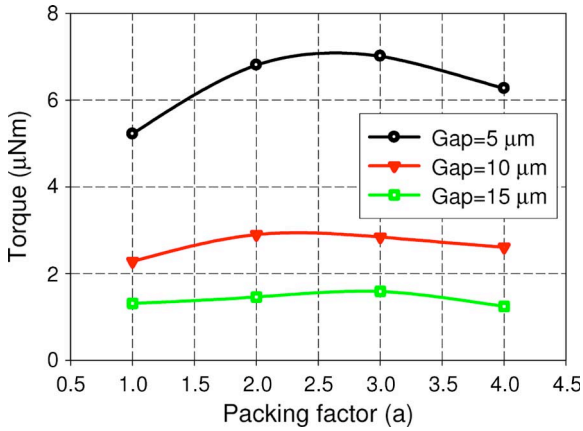

Fig. 5. Estimated torque as a function of the geometry and the gap for four different designs at $V = 100$ V. With the gap of 10 μm, the torque is about 3 μN $\cdot$ m for the two primary designs, i.e., $a = 2$ and $a = 3$.

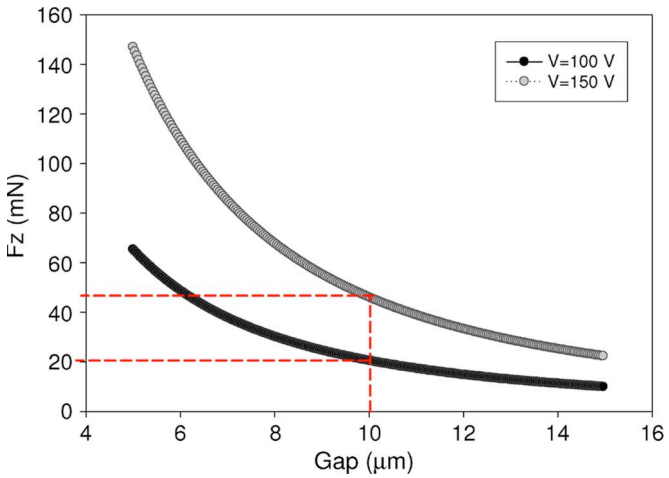

Fig. 6. Absolute value of the normal force as a function of the gap size. The estimated normal force of the motor with $G = 10$ μm and $V = 100$ V is 20.5 mN.

15 μm is more feasible than 5 μm. The values shown in Fig. 5 will be increased by a factor of 2.25 if the excitation voltage is increased from 100 to 150 V. The maximum excitation voltage is limited by the instrumentation and the dielectric breakdown. Based on the simulation results, the packing factors of two and three, which produce the highest torque, are chosen.

The torque is the result of the tangential force on the rotor produced by the electric field and determines the load-driving performance of the machine. The electric field also produces a normal force on the rotor that stabilizes and holds the rotor on the stator. This force affects the frictional torque on the rotor and is calculated. The FE simulations were performed to estimate change in the capacitance with respect to the gap. The normal force (F_z) can be estimated as

$$F_z = -\frac{1}{2}V^2\frac{\mathrm{d}C_{\mathrm{Max}}(z)}{\mathrm{d}z} \tag{3}$$

where z is normal to rotor plane. Fig. 6 shows the simulation results of the normal force versus the gap size for a machine with $a = 3$ and $N_e = 138$. As shown in the graph, the estimated normal force for the gap size of 10 μm and the excitation of 100 V is 20.5 mN which is approximately ten times higher than the gravitation force on the rotor (0.2-g mass).

Based on these simulation results and fabrication limitations, micromotors with different geometries are designed. Table I shows the summary of the design parameters.

TABLE I
GEOMETRY SPECIFICATIONS FOR TWO PRIMARY DESIGNS

Specification	Value
Electrode thickness (nm)	270
Spacing between adjacent electrodes (μm)	30/45
Number of electrodes	156/138
Number of poles	104/92
Pole/housing depth on rotor(μm)	135
Housing depth on stator(μm)	130
Microball diameter (μm)	284.5
Microball housing width (μm)	290
Air gap (μm)	10
Active area inner radius(mm)	1.0
Active area outer radius (mm)	5.0
Microball housing inner radius (mm)	5.8
Outer rotor radius (mm)	7.0

III. FABRICATION

The fabrication processes of the stator and the rotor of the micromotor use seven and two mask levels, respectively. Figs. 7 and 8 show the schematic cross sections of the stator and the rotor during the fabrication process, respectively. The stator fabrication starts with etching 5.8-μm-deep alignment marks in a silicon substrate (p-type, $\langle 100\rangle$, $\rho = 1 - 10\ \Omega \cdot$ cm, and 525 ± 25 μm thick) using reactive-ion-etching (RIE) tool (Trion Technologies). A 3.2-μm-thick photosensitive BCB film (Cyclotene 4022–35 from Dow Chemical) is then deposited to isolate the active parts of the machine from the silicon substrate. The BCB film is partially cured (at 212° for 40 min) in a nitrogen environment followed by a 30-s-long O_2/CF_4 plasma etch (descum) to remove polymer residues. The residual stress of the BCB film is measured to be 29 MPa (tensile) on test wafers.

A 20/250-nm-thick chromium (Cr)/gold (Au) layer is then deposited using a dc magnetron sputtering system (AJA International) at 5 mtorr (0.66 Pa) and 50 W. The metal layer is patterned using a positive photoresist (AZ9245) and two wet-etching steps. This layer forms the interconnection level that connects every sixth electrode of the six-phase machine.

The second photosensitive BCB layer with a thickness of 2.8 μm is then spun, patterned, partially cured, and descummed to form an ILD film with open vias for electrical connection between the two metal layers. The thickness of this layer is chosen such that the conformal BCB film prevents any possible dielectric breakdown between the metal layers particularly at sharp metal edges. Previously, when a metal thickness of 0.5 μm and a BCB thickness of $1-2$ μm were used, electric-breakdown failure was observed. To address this problem and to increase process yield, a metal thickness of 0.27 μm and a BCB thickness of 2.8 μm were used after a careful process characterization. A 1.6-μm-thick image reversal photoresist (AZ5214E)

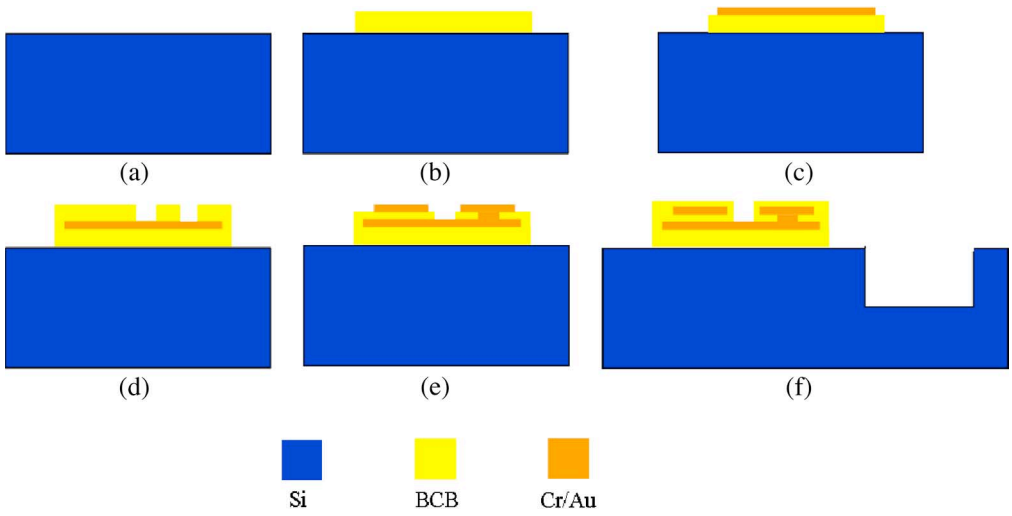

Fig. 7. Cross-sectional schematics showing the stator fabrication process. (a) Silicon wafer. (b) BCB deposition and lithography. (c) Metal deposition. (d) BCB deposition and lithography (via formation). (e) Metal deposition. (f) Metal housing etch.

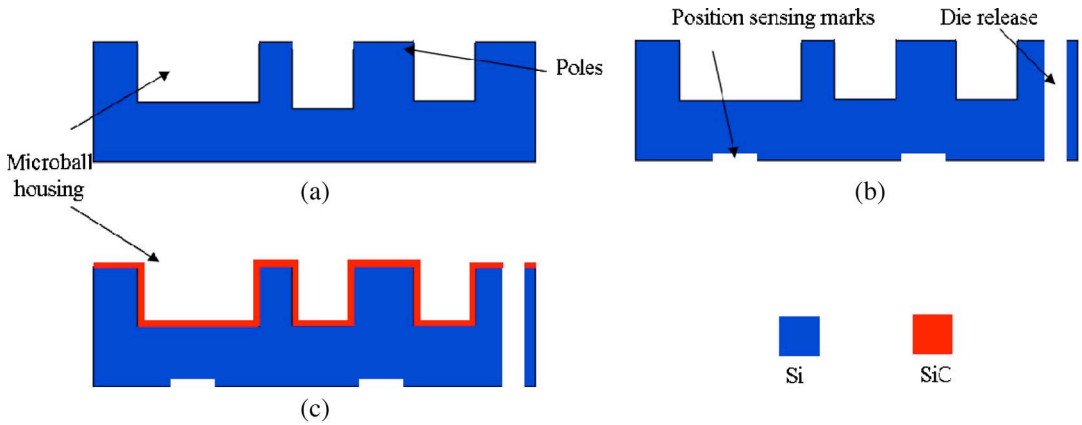

Fig. 8. Cross-sectional schematics showing the rotor fabrication process. (a) Front side etch to create poles and microball housing. (b) Etch from the back side to release the die and create marks for position sensing. (c) Silicon carbide deposition.

is then patterned, a 20/250-nm-thick Cr/Au layer is sputtered, and the metal is subsequently lifted off in acetone and deionized water using an ultrasonic bath. The electrical resistance between the electrode and the interconnection layers and the sheet resistance of each metal layer are measured to be $23-47\ \Omega$ and $416\ \mathrm{m}\Omega/\mathrm{sq}$, respectively.

The third BCB film is then deposited, patterned, partially cured, and descummed to form a 2.0-μm-thick passivation layer. This layer protects the active parts of the machine from contamination and electric breakdown during testing or operation. The microball housings are then etched $132.4 \pm 0.4\ \mu$m deep in the silicon substrate using a 9-μm-thick photoresist mask (AZ9245) and a deep RIE (DRIE) tool (Surface Technology Systems). The BCB films are cured at 250 °C for 1 h to reach 95%–100% polymerization. In the last step of the stator fabrication, a 30-s-long O_2/CF_4 plasma etch is performed. This step removes any residue from the contact pads to enhance the electrical connection to the probes. Fig. 9(a)–(c) shows different sections of the fabricated stator. A total of 17 devices are fabricated on the stator wafer.

The rotor fabrication process starts with a DRIE step to form salient poles and microball housing on one side of the wafer. The housing depth is measured to be $135.5 \pm 0.4\ \mu$m. Then, the wafer DRIE step is performed on the other side of the wafer to release the rotor, etch the center opening, and etch marks for position detection. Finally, a 173 ± 20-nm-thick film of SiC is deposited on the rotor dies using RF magnetron sputtering. The deposition is performed at the room temperature with pressure and power of 2.5 mtorr (0.33 Pa) and 300 W, respectively. Fig. 9(d)–(f) shows the fabricated rotor after release and before the SiC deposition. A total of six devices are fabricated on the rotor wafer. To reduce the depth nonuniformity of the microball housings, only six devices per wafer are designed to minimize the DRIE loading. Based on the depth measurements of the housings on the rotor and the stator, as well as the measurement of the stator film structure thickness, the air gap was estimated to be $10-13\ \mu$m.

After the completion of the fabrication process, the stator is clamped to an aluminum chuck. A total of ten stainless-steel microballs, each $284.5 \pm 0.25\ \mu$m in diameter (Thomson Precision Balls), are manually positioned inside the stator trench using tweezers. The rotor is then manually aligned and positioned on top of the stator. If the rotor is aligned and positioned properly, it rotates freely with little resistance.

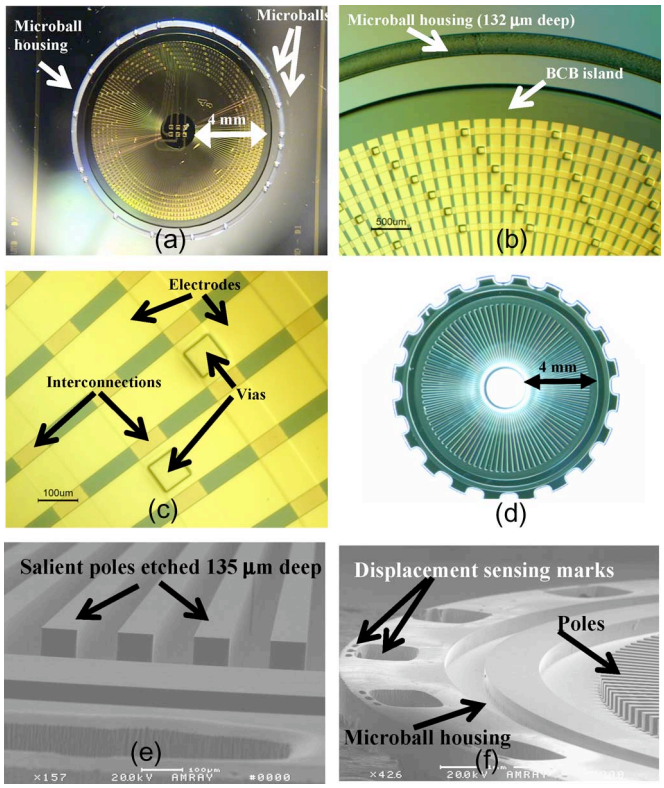

Fig. 9. Fabricated (a) stator, (b) outer radius of the stator, (c) two-level metallization and vias, (d) rotor with 104 poles, (e) rotor poles, and (f) outer radius of the rotor.

IV. Characterization

A. Test Setup

A characterization methodology is developed to measure and extract the angular displacement, velocity, acceleration, torque, mechanical power, coefficient of friction, and frictional force for the micromotors through noncontact techniques. These measurements are discussed in this section. The block diagram of the setup used for exciting the motor and tracking the motion is shown in Fig. 10. The micromotor is excited using a six-phase high-voltage system composed of a PC, a LabView interface, a data-acquisition card, and a high-voltage amplifier with a maximum output voltage of ± 150 V. The excitation signals are applied to the stator using six micropositioners with tungsten-probe tips (Fig. 11).

As shown in the block diagram of Fig. 10, two schemes were implemented for measuring the displacement of the rotor. The first method utilizes an optical displacement sensor (Model D6 from Philtech) to detect 20 silicon pits etched in the rotor. The sensor is mounted on an $X-Z$ micropositioning stage. This method provides an accurate measurement for the average angular velocity. The assembled micromotor and the test setup are shown in Fig. 12. The second method utilizes a high-speed charged-coupled-device camera (Model HS-3 from Redlak) together with a microscopic lens (Model KV from Infinity Photo-Optical Company) to measure the transient response of the machine with a temporal resolution of 1 ms. The recorded images are processed using a commercial tracking software (ProAnalyst from Xcitex). This real-time measurement approach was preferred over stroboscopic dynamometry techniques previously used for side-drive micromotors [30] due to the greater displacement and temporal accuracy.

B. Steady-State Response

One of the characteristics of any synchronous motor is the synchronization of the mechanical motion of the rotor with the electrical excitation of the stator. A series of experiments is performed to test the angular velocity of the rotor versus the excitation frequency for the two designs discussed earlier: D1 with 104 poles $(a = 3)$ and D2 with 92 poles $(a = 2)$. The velocity of the rotor is measured using the optical displacement sensor. Fig. 13(a) and (b) shows the experimental results together with the theoretical values for D1 and D2, respectively. A top velocity of 517 r/min, corresponding to the linear tip velocity of 324 mm/s, is measured for D2. The top measured velocity for D1 is 454 r/min. As shown in this figure, there is an excellent agreement between the measured and predicted angular velocities. The achieved velocity is about 44 times higher than the maximum velocity measured (7.2 mm/s) for the second-generation linear device [25] supported on the microball bearings.

C. Transient Response

The coefficient of friction between the stainless-steel microballs, the silicon housing on the stator, and the SiC housing on the rotor, as well as the torque of the machine, can be indirectly obtained from transient response measurements. In this method, the excitation voltage is set to 0 V at $t = 0$, and the deceleration of the rotor is extracted from angular-position measurement using the high-speed camera system described earlier. The friction force can be modeled as the product of the normal force and the coefficient of friction (μ). By assuming that the friction is the dominate loss mechanism, it can be shown that the μ and the angular acceleration (α) are related [29] by

$$\mu = \frac{T_{\text{Friction}}}{MgR_0} = \frac{\alpha I}{MgR_0} = \frac{\alpha \frac{1}{2} M\left(R_1^2 + R_2^2\right)}{MgR_0} = \underbrace{\frac{R_1^2 + R_2^2}{2gR_0}}_{\text{const.}} \alpha \tag{4}$$

where R_0, R_1, and R_2 are the bearing radius, the rotor inner radius, and the rotor outer radius, respectively, and M and I are the rotor mass and the moment of inertia, respectively. By assuming that the μ is not a function of the normal force (F_{N}), the torque (T_{EM}) of the micromotor at $V = V_0$ is equal to the frictional torque at a constant angular velocity. Therefore

$$T_{\text{EM}}\,|_{V=V_0} = \underbrace{\frac{F_{\text{N}}(V_0)\left(R_1^2 + R_2^2\right)}{2g}}_{\text{const.}} \alpha \tag{5}$$

where V_0 is the minimum voltage at which the micromotor is operational. $F_{\text{N}}(V_0)$ is estimated from the FE simulation results discussed earlier. Fig. 14 shows the measured angular position

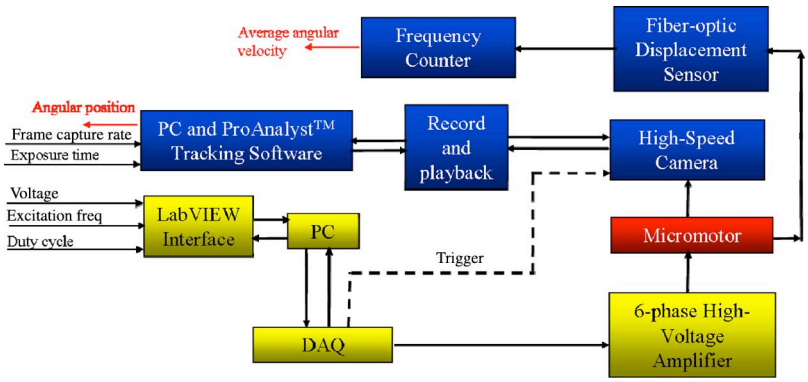

Fig. 10. Block diagram of the micromotor characterization setup.

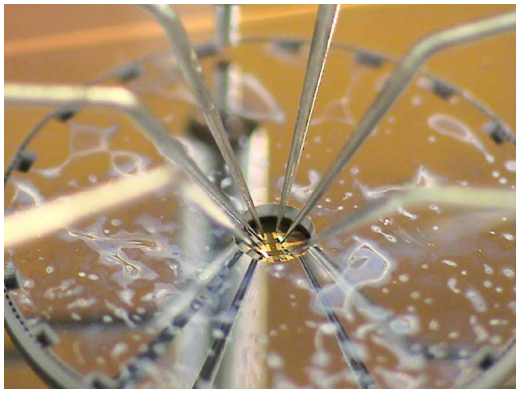

Fig. 11. Electrical connection to the stator is provided by six probes through the 2-mm-diameter rotor opening. The residues on the backside of the rotor are a result of wafer bonding and DRIE steps.

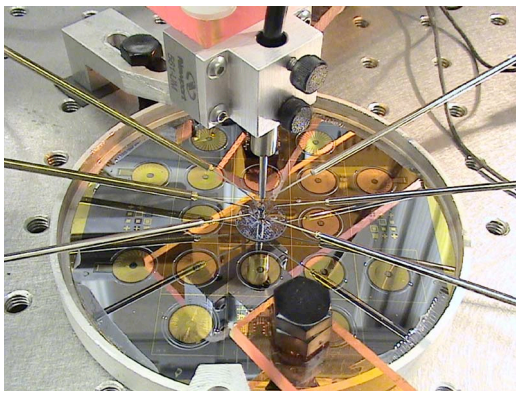

Fig. 12. Picture of the micromotor under test.

of the rotor as a function of the time $(0 < t < 1\ \mathrm{s})$ when the excitation voltage is set to zero at $t = 0$. This is made possible by synchronizing the camera's capture sequence with the excitation signal. For $t < 0$, the machine is excited at the fixed frequency of 300 Hz, corresponding to the constant angular velocity of 20.5 rad/s. Once the voltage is set to zero, the rotor starts to decelerate until it completely stops due to friction. The extracted deceleration is used in conjunction with (4) to calculate μ. Deceleration, by itself, is calculated as follows. The measured position data $\theta(t)$ are fitted to an exponential function (curve fit using MATLAB) in the form of $\theta = ae^{bt} + ct + d$ with a standard coefficient of determination of 0.9999, where a, b, c, and d are constants. This exponential function is the solution to the differential equation of motion, assuming that the angular acceleration is a linear function of angular velocity plus a constant. The angular velocity and the acceleration are then computed through numerical differentiation of $\theta(t)$. The value of the computed velocity at the onset of turn off $\dot{\theta}(t = 0)$ is 20.5 rad/s which is identical to the measured steady-state velocity before turn off. Fig. 15 shows the computed angular acceleration which is used in conjunction with (4) and (5) to extract the torque and the coefficient of friction. The extraction of torque and coefficient of friction from the deceleration of the rotor relies on the correct and repeatable measurement of the acceleration (α). Fig. 15 shows three separate measurements when the excitation frequencies of stator are 200 and 300 Hz. As shown in Fig. 15, the error between the three measurements is about 10%. This implies that the torque and friction measurements have a minimum error of 10%. These correction factors are added in Table II. The torque also relies on the accurate estimation of the normal force which is derived from the simulation results.

Based on this analysis, the torque of the machine at $V = 150$ V is indirectly measured to $-5.62 \pm 0.5\ \mu\mathrm{N} \cdot \mathrm{m}$. This value is comparable with the FE simulation result of $-6.75\ \mu\mathrm{N} \cdot \mathrm{m}$ discussed earlier $(\mathrm{gap} = 10\ \mu\mathrm{m})$. Similarly, the bearing coefficient of friction is calculated to be 0.0196 ± 0.002. Based on the torque measurement results, the maximum mechanical output power of the motor is calculated to be 307 μW at 517 r/min. Table II summarizes the geometric factors and the measurement results, including the frictional torque and force for D2.

V. Discussion

A number of observations have been made during the micromotor testing that reveal information about the microball bearings as well as the inherent characteristics of the designed VCM. The first series of experiments were performed without SiC coating on the rotor; none of the two designs was operational. However, both designs were proven to operate reliably after the deposition of SiC coating on the rotor. It is believed that the hard SiC film reduces the frictional torque such that the torque becomes sustainable by the machine.

Experiments were performed to verify the number of balls needed for a reliable operation. It has been observed that for

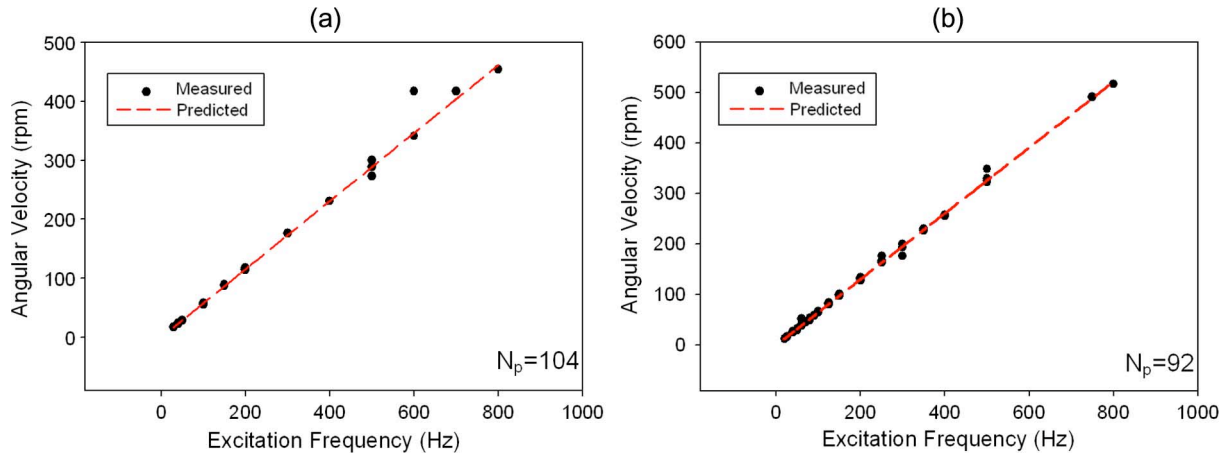

Fig. 13. Angular velocity versus excitation frequency for a micromotor with (a) 104 poles and (b) 92 poles shows a good agreement between the predicted and measured velocities.

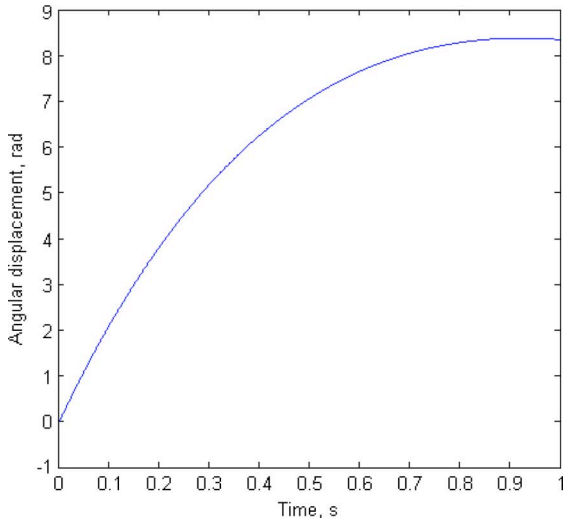

Fig. 14. Angular position of the rotor as a function of time after the excitation is set to $\nu = 0$ at $t = 0$ s.

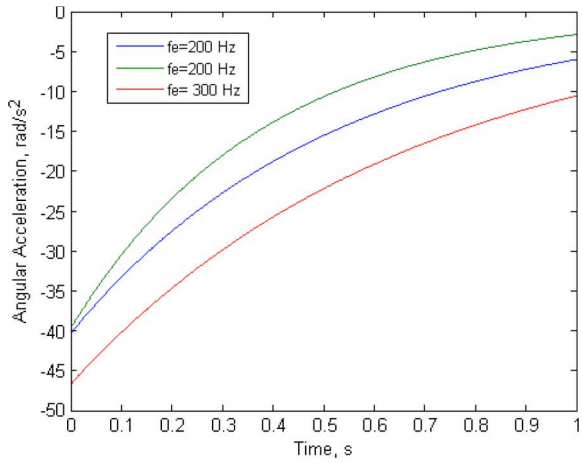

Fig. 15. Angular acceleration (α) of the rotor is derived from time differentiation (twice) of the angular position (f_e is the excitation frequency before turn off).

D1 and D2, about ten microballs result in a reliable operation, whereas less than ten can cause a quick ball colocation (jamming) and higher than 15 results in high friction that halts the operation. The number of balls used in the bearing affects the effective contact area as well as the normal loading carried by each ball. Low number of balls results in instability due to the continuous bearing design. This limitation can be addressed in the future by segmenting the bearing. A friction study that takes ball loading, surface area, velocity, and number of used balls is currently underway in our group on less complicated MEMS structures.

The higher achieved velocity for the rotary VCM, compared with the linear counterparts, is due to the nature of the rotary motion (continuous momentum and motion) as well as the improvements made in the design and fabrication of the micromotor, including the etch uniformity of microball housings and the use of SiC film as a dry lubricant. One of the obstacles in achieving higher velocities is the colocation of the balls and the ball-to-ball collisions. This can cause a sudden spike in friction, gap nonuniformity, and jamming. The higher the angular velocity of the rotor, the faster the colocation of the balls is observed. A higher angular velocity (>517 r/min), however, would be achievable by using a closed-loop excitation system. Using lubricant films, such as SiC and diamondlike carbon, on both the stator and the rotor housings to further reduce the friction and incorporating a retainer ring to eliminate the ball-to-ball collision and the ball colocation will also help achieve higher velocities. These issues will be addressed in the future generation of these devices.

The test results presented here are all performed at $\pm$150-V excitation which is the maximum achievable amplitude of the high-voltage amplifier that we used. None of the designs demonstrated a reliable performance when excited below this value. This suggests that the power angle of this synchronous motor is at the critical value when excited by $\pm$150 V; therefore, the calculated torque extracted through friction measurements truly represents the maximum sustainable torque by the machine. In addition, the measured torque value of -5.62 ± 0.5 μN $\cdot$ m is in agreement with the FE simulation result of -6.75 μN $\cdot$ m for a machine with a 10-μm gap. Due to the fabrication limitations and imperfections, the fabricated micromotor has the gap of $10-13$ μm which explains the difference between the predicted and measured torques. The measured torque of -5.62 μN $\cdot$ m is substantially higher

TABLE II
SUMMARY OF THE ELECTROMECHANICAL TORQUE OF THE MACHINE (DESIGN D2) AT 150 V, COEFFICIENT OF FRICTION, FRICTIONAL TORQUE AT NO VOLTAGE, AND THE CONSTANTS USED IN THE CALCULATION

R_1 (mm)	R_2 (mm)	R_0 (mm)	g (m/s^2)	F_N @ 150V (mN)	α (rad/s^2)
1	7	6	9.8	48	-46
I (kg m^2)	M (kg)	T_{EM} @ 150 V (μN·m)	$T_{Friction}$ @ 0V (μN·m)	$F_{Friction}$ @ 0V (μN)	μ
4.70×10^{-9}	1.88×10^{-4}	-5.62 ± 0.5	0.22 ± 0.02	36.0 ± 3	0.0196± 0.002

compared with the torques reported for other micromotors such as 12 pN · m for the conventional side-drive VCMs [10], 3.5 μN · m for the induction micromotors supported on gas-lubricated bearings [11], [12], and 2.5 μN · m for the magnetic induction micromotors with tethered rotors [13]. This is the direct result of a careful geometry design that includes 75 mm^2 of active area and small air gap of 10 μm which would not have been possible without the microball-bearing technology.

The tested micromotor has a total radius of 7 mm which makes the characterization less complex compared with the smaller motors. It is possible to reduce the device footprint in future designs. The torque is proportional to the active area and scales down with the square of radius. The angular velocity is proportional to the excitation frequency and inversely proportional to the number of poles. Therefore, the scale-down does not necessarily affect the velocity as long as the number of poles is kept constant. When a smaller device is designed, the gap can be reduced below the current size of 10 μm to compensate for the torque. However, smaller gap sizes impose new fabrication challenges.

The derived coefficient of friction of 0.0196 $\pm$ 0.002 is comparable to the reported coefficient of 0.007–0.01 for the silicon housings (v-grooves) etched using potassium hydroxide [20], [23]. In all the experiments discussed here, ten microballs are used; therefore, the average load on each contact point is about 20 mg. Different loading conditions, housing geometry/material, number of housings, number of balls, and test conditions (e.g., humidity) are all expected to affect the coefficient of friction. Even though the device is not packaged, experimental results performed at the room environment (outside the clean room) have proven the reliability of the device operating for a number of hours at low speeds ($\sim$17 r/min).

VI. CONCLUSION

The successful development of the first rotary micromotor supported on the microball bearings is reported in this paper. The micromotor is a six-phase variable-capacitance machine with a bottom-drive design resulting in a large active area and a large torque. One of the major challenges in the development of electric micromachines in the past has been the robustness of the rotor's mechanical support which has been addressed in this paper. The microball-bearing technology provides a uniform and small air gap and a robust mechanical support for the rotor. The results illustrate that coating the rotor with the SiC film is crucial for the operation of the machine due to the reduction of friction. A top angular velocity of 517 r/min is measured corresponding to a linear tip velocity of 324 mm/s; this is 44 times higher than the top velocity measured for the linear device (7.2 mm/s). The electromechanical torque is indirectly measured for the excitation voltage of $\pm$150 V to be -5.62 ± 0.5 μN · m which is comparable with the simulation result of -6.75 μN · m. The maximum output mechanical power at $\pm$150 V and 517 r/min is calculated to be 307 μW. The housing coating with SiC film is proven to be highly effective in reducing the friction. The coefficient of friction for the bearings is measured to be 0.02 $\pm$ 0.002 which is in good agreement with the previously reported values [20]. The rotary micromotor developed in this paper is a platform technology for a number of power MEMS devices, including a centrifugal micropump used in fuel-delivery and cooling applications.

ACKNOWLEDGMENT

The authors would like to thank the members of the MEMS Sensors and Actuators Laboratory, University of Maryland, especially Dr. M. McCarthy, for their feedback and assistance. The authors would also like to thank Dr. J. O'Connor, T. Loughran, and J. Hummel of the Maryland Nanocenter clean room facilities (FabLab) and C. Mike Waits of the Army Research Laboratory, Adelphi, MD, for their help with the fabrication of devices.

REFERENCES

[1] D. J. Laser and J. G. Santiago, "A review of micropumps," *J. Micromech. Microeng.*, vol. 14, no. 6, pp. R35–R64, Jun. 2004.
[2] T. Weisener, G. Vogele, M. Widmann, C. Bark, R. D. Schraft, A. Bertholds, and A. Braunschweiler, "Development and fabrication of a rotary micropump and its industrial and medical applications," in *Proc. SPIE*, Austin, TX, 1996, pp. 218–225.
[3] C. H. Ahn and M. G. Allen, "Fluid micropumps based on rotary magnetic actuators," in *Proc. IEEE MEMS*, Amsterdam, The Netherlands, 1995, p. 408.
[4] B. Mladen, J. M. Jack, P. G. Andrew, and S. Schultz, "Electromagnetic micromotor for microfluidics applications," *Appl. Phys. Lett.*, vol. 79, no. 9, pp. 1399–1401, Aug. 2001.
[5] X. Wang, S. Cui, and S. Cheng, "Advantages of electrostatic micromotor and its application to medical instruments," in *Conf. Rec. IAS Annu. Meeting*, Pittsburgh, PA, 2002, pp. 2466–2468.
[6] D. Polla, A. Erdman, D. Peichel, R. Rizq, Y. Gao, and D. Markus, "Precision micromotor for surgery," in *Proc. 1st Annu. Int. IEEE-EMBS Special Topic Conf. Microtechnologies Med. Biol.*, Lyon, France, Oct. 12–14, 2000, pp. 180–183.
[7] S. Fatikow, A. Falzullin, and J. Seyfried, "Planning of a microassembly task in a flexible microrobot cell," in *Proc. IEEE ICRA*, San Francisco, CA, Apr. 24–28, 2000, pp. 1121–1126.
[8] R. Yeh, S. Hollar, and K. S. J. Pister, "Design of low-power silicon articulated microrobots," *J. Micromechatronics*, vol. 1, no. 3, pp. 191–203, 2002.

[9] R. Yeh, E. J. J. Kruglick, and K. S. J. Pister, "Surface-micromachined components for articulated microrobots," *J. Microelectromech. Syst.*, vol. 5, no. 1, pp. 10–17, Mar. 1996.
[10] M. Mehregany, S. F. Bart, L. S. Tavrow, J. H. Lang, and S. D. Senturia, "Principles in design and microfabrication of variable-capacitance side-drive motors," *J. Vac. Sci. Technol. A, Vac., Surf., Films*, vol. 8, no. 4, pp. 3614–3624, Jul./Aug. 1990.
[11] S. F. Nagle, C. Livermore, L. G. Frechette, R. Ghodssi, and J. H. Lang, "An electric induction micromotor," *J. Microelectromech. Syst.*, vol. 14, no. 5, p. 1127, Oct. 2005.
[12] C. Livermore, A. R. Forte, T. Lyszczarz, S. D. Umans, A. A. Ayon, and J. H. Lang, "A high-power MEMS electric induction motor," *J. Microelectromech. Syst.*, vol. 13, no. 3, pp. 465–471, Jun. 2004.
[13] D. P. Arnold, S. Das, F. Cros, I. Zana, M. G. Allen, and J. H. Lang, "Magnetic induction machines integrated into bulk-micromachined silicon," *J. Microelectromech. Syst.*, vol. 15, no. 2, pp. 406–414, Apr. 2006.
[14] J. L. Steyn and J. H. Lang, "Generating electric power with a MEMS electroquasistatic induction turbine-generator," in *Proc. IEEE MEMS*, Miami, FL, 2005, pp. 614–617.
[15] D. P. Arnold, H. Florian, Z. Iulica, G. Preston, P. Jin-Woo, D. Sauparna, H. L. Jeffrey, and G. A. Mark, "Design optimization of an 8 W, microscale, axial-flux, permanent-magnet generator," *J. Micromech. Microeng.*, vol. 16, no. 9, pp. S290–S296, Sep. 2006.
[16] D. P. Arnold, S. Das, J. W. Park, I. Zana, J. H. Lang, and M. G. Allen, "Microfabricated high-speed axial-flux multiwatt permanent-magnet generators—Part II: Design, fabrication, and testing," *J. Microelectromech. Syst.*, vol. 15, no. 5, pp. 1351–1363, Oct. 2006.
[17] W. Zhang, G. Meng, and H. Li, "Electrostatic micromotor and its reliability," *Microelectron. Reliab.*, vol. 45, no. 7/8, pp. 1230–1242, Jul./Aug. 2005.
[18] W. Chee Wei, Z. Xin, S. A. Jacobson, and A. H. Epstein, "A self-acting gas thrust bearing for high-speed microrotors," *J. Microelectromech. Syst.*, vol. 13, no. 2, pp. 158–164, Apr. 2004.
[19] L. G. Frechette, S. A. Jacobson, K. S. Breuer, F. F. Ehrich, R. Ghodssi, R. Khanna, W. Chee Wei, Z. Xin, M. A. Schmidt, and A. H. Epstein, "High-speed microfabricated silicon turbomachinery and fluid film bearings," *J. Microelectromech. Syst.*, vol. 14, no. 1, pp. 141–152, Feb. 2005.
[20] L. Ta-Wei, A. Modafe, B. Shapiro, and R. Ghodssi, "Characterization of dynamic friction in MEMS-based microball bearings," *IEEE Trans. Instrum. Meas.*, vol. 53, no. 3, pp. 839–846, Jun. 2004.
[21] A. Modafe, N. Ghalichechian, A. Frey, J. H. Lang, and R. Ghodssi, "Microball-bearing-supported electrostatic micromachines with polymer dielectric films for electromechanical power conversion," in *Proc. Power MEMS*, Tokyo, Japan, 2005, pp. 173–176.
[22] Y.-C. Tai, L.-S. Fan, and R. S. Muller, "IC-processed micro-motors: Design, technology, and testing," in *Proc. IEEE Micro Electro Mech. Syst.*, Salt Lake City, UT, 1989, pp. 1–6.
[23] X. Tan, A. Modafe, and R. Ghodssi, "Measurement and modeling of dynamic rolling friction in linear microball bearings," *J. Dyn. Syst., Meas. Control*, vol. 128, no. 4, pp. 891–898, Dec. 2006.
[24] A. Modafe, N. Ghalichechian, A. Frey, J. H. Lang, and R. Ghodssi, "Microball-bearing-supported electrostatic micromachines with polymer dielectric films for electromechanical power conversion," *J. Micromech. Microeng.*, vol. 16, no. 9, pp. S182–S190, Sep. 2006.
[25] N. Ghalichechian, A. Moadafe, and R. Ghodssi, "Dynamic characterization of a linear electrostatic micromotor supported on microball bearings," *Sens. Actuators A, Phys.*, vol. 136, no. 2, pp. 416–503, May 2007.
[26] A. Modafe, N. Ghalichechian, M. Powers, M. Khbeis, and R. Ghodssi, "Embedded benzocyclobutene in silicon: An integrated fabrication process for electrical and thermal isolation in MEMS," *Microelectron. Eng.*, vol. 82, no. 2, pp. 154–167, Oct. 2005.
[27] N. Ghalichechian, A. Modafe, R. Ghodssi, P. Lazzeri, V. Micheli, and M. Anderle, "Integration of benzocyclobutene polymers and silicon micromachined structures using anisotropic wet etching," *J. Vac. Sci. Technol. B, Microelectron. Process. Phenom.*, vol. 22, no. 5, pp. 244–2439, Sep. 2004.
[28] N. Ghalichechian, A. Modafe, M. I. Beyaz, C. M. Waits, and R. Ghodssi, "Design and fabrication of a rotary electrostatic micromotor supported on microball bearings," in *Proc. Power MEMS*. Berkeley, CA, 2006, pp. 227–230.
[29] N. Ghalichechian, "Design, fabrication, and characterization of a rotary micromotor supported on microball bearings," Ph.D. dissertation, Dept. Elect. Comput. Eng., Univ. Maryland, College Park, MD, 2007.
[30] S. F. Bart, M. Mehregany, L. S. Tavrow, J. H. Lang, and S. D. Senturia, "Electric micromotor dynamics," *IEEE Trans. Electron Devices*, vol. 39, no. 3, pp. 566–575, Mar. 1992.

Nima Ghalichechian (S'99) received the B.S. degree in electrical engineering from Amirkabir Institute of Technology (Tehran Polytechnique), Tehran, Iran, in 2001. His B.S. thesis was focused on design and fabrication of a maximum power point tracking circuit for photovoltaics. In 2002, he started his graduate studies at the University of Maryland, College Park, MD. For his Master's research, he developed new MEMS fabrication processes to fabricate an electrostatic micromotor and performed metal-polymer adhesion and interface studies. He received the M.S. degree in 2005, with a thesis titled "Integration of Benzocyclobutene Polymers and Silicon Micromachined Structures Fabricated with Anisotropic Wet Etching." For his Ph.D. research, he developed the first rotary micromotor supported on microball bearings. He also developed linear micromotors supported on microball bearings. He received the Ph.D. degree in 2007, with a dissertation titled "Design, Fabrication, and Characterization of a Rotary Variable-Capacitance Micromotor Supported on Microball Bearings." This micromotor is a platform for developing micropumps and microgenerators.

He is currently with the MEMS Research Group at Formfactor Inc., Livermore, CA.

Alireza Modafe (S'01) was born in Lahijan, Iran, in 1970. He received the B.S. degree in electrical engineering from Sharif University of Technology, Tehran, Iran, in 1993, the M.S. degree in electrical engineering from Iran University of Science and Technology, Tehran, Iran, in 1997, and the Ph.D. degree in electrical engineering from the University of Maryland (UMD), College Park, MD, in 2007. His Ph.D. dissertation was focused on design, fabrication, and characterization of benzocyclobutene (BCB)-based electrostatic micromachines supported on microball bearings.

He was a Research Assistant with the MEMS Sensors and Actuators Laboratory, Department of Electrical and Computer Engineering, Institute for Systems Research, UMD, from 2000 to 2006. His research resulted in the development of the first microball-bearing-supported micromotor with BCB insulating layers. Since April 2007, he has been with the Micron Technology Inc., Manassas, VA, where he works as a Product Engineer in the DRAM Product and Quality Assurance Engineering Group.

Dr. Modafe is a member of the American Vacuum Society and the Materials Research Society, and he is also an Associate Member of Sigma Xi, The Scientific Research Society. He was the recipient of the 2002 Spring MEMS Alliance Workshop Best Poster Award and the 2002 AVS Graduate Research Award.

Mustafa Ilker Beyaz (S'07) received the B.S. degree in electrical and electronics engineering from the Middle East Technical University, Ankara, Turkey, in 2005. He is currently working toward the M.S. and Ph.D. degrees under the guidance of Prof. Reza Ghodssi in the MEMS Sensors and Actuators Laboratory, Department of Electrical and Computer Engineering, Institute for Systems Research, University of Maryland, College Park, MD.

His research interests include design, fabrication, and characterization of power MEMS devices, micromachine control systems, and microgenerators.

Reza Ghodssi (M'92) received the B.S., M.S., and Ph.D. degrees in electrical engineering from the University of Wisconsin, Madison, in 1990, 1992, and 1996, respectively.

He was a Postdoctoral Associate and a Research Scientist with the Microsystems Technology Laboratories and the Gas Turbine Laboratory, Massachusetts Institute of Technology, Cambridge, from 1997 to 1999. He is currently an Associate Professor and the Director of the MEMS Sensors and Actuators Laboratory, Department of Electrical and Computer Engineering, Institute for Systems Research, University of Maryland (UMD), College Park, MD. He is also affiliated with the Fischell Department of Bioengineering, the Maryland NanoCenter, the University of Maryland Energy Research Center, and the Materials Science and Engineering Department at UMD. He has over 55 scholarly publications and is the Editor of the "Handbook of MEMS Materials and Processes" to be published in 2009. His research interests include the design and development of integrated micro/nanosystems for chemical and biological sensing, small-scale energy conversion, and harvesting.

Dr. Ghodssi is the Cofounder of MEMS Alliance in the greater Washington area and a member of the American Vacuum Society, the Materials Research Society, the American Society for Engineering Education, and the American Association for the Advancement of Science. He was the recipient of the 2001 UMD George Corcoran Award, the 2002 National Science Foundation CAREER Award, and the 2003 UMD Outstanding Systems Engineering Faculty Award. He was among 83 of the nation's outstanding engineers (aged 30–45) invited to attend the National Academy of Engineering 2007 U.S. Frontiers of Engineering Symposium in Redmond, WA.